

RD-A194 687

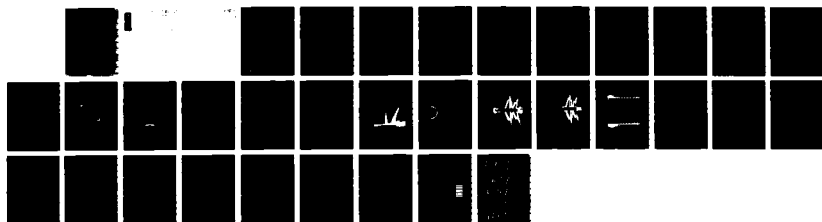
NUMERICAL SIMULATION OF THREE DIMENSIONAL TRANSONIC  
FLOWS (U) ARMY BALLISTIC RESEARCH LAB ABERDEEN PROVING  
GROUND MD J SAHU ET AL. MAR 88 BRL-TR-2963

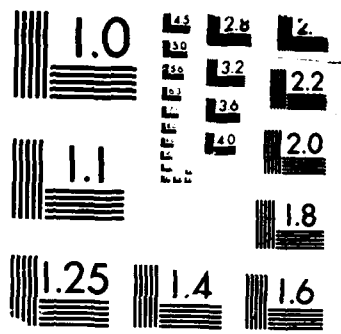
1/1

UNCLASSIFIED

F/G 20/4

ML





MICROCOPY RESOLUTION TEST CHART

IRFAN U. STANDARDS-1963-A

ADA194687

Form Approved  
OMB No. 0704-0188

REPORT DOCUMENTATION PAGE					
1a. REPORT SECURITY CLASSIFICATION UNCLASSIFIED		1b. RESTRICTIVE MARKINGS			
2a. SECURITY CLASSIFICATION AUTHORITY		3. DISTRIBUTION/AVAILABILITY OF REPORT Approved for public release, distribution unlimited.			
2b. DECLASSIFICATION/DOWNGRADING SCHEDULE					
4. PERFORMING ORGANIZATION REPORT NUMBER(S)  BRL-TR-2903		5. MONITORING ORGANIZATION REPORT NUMBER(S)			
6a. NAME OF PERFORMING ORGANIZATION U.S. Army Ballistic Research Laboratory		6b. OFFICE SYMBOL (If applicable) SLCBR-LF	7a. NAME OF MONITORING ORGANIZATION		
6c. ADDRESS (City, State, and ZIP Code)  Aberdeen Proving Ground, Maryland 21005-5066		7b. ADDRESS (City, State, and ZIP Code)			
8a. NAME OF FUNDING/SPONSORING ORGANIZATION		8b. OFFICE SYMBOL (If applicable)	9. PROCUREMENT INSTRUMENT IDENTIFICATION NUMBER		
8c. ADDRESS (City, State, and ZIP Code)		10. SOURCE OF FUNDING NUMBERS			
		PROGRAM ELEMENT NO. 61102A	PROJECT NO. 1L161102AH43	TASK NO. 00	WORK UNIT ACCESSION NO. 001 AJ
11. TITLE (Include Security Classification)  NUMERICAL SIMULATION OF THREE DIMENSIONAL TRANSONIC FLOWS					
12. PERSONAL AUTHOR(S) SAHU, JUBARAJ and STEGER, JOSEPH L.*					
13a. TYPE OF REPORT Technical Report		13b. TIME COVERED FROM _____ TO _____	14. DATE OF REPORT (Year, Month, Day)		15. PAGE COUNT
16. SUPPLEMENTARY NOTATION *NASA Ames Research Center Moffett Field, CA 94035					
17. COSATI CODES		18. SUBJECT TERMS (Continue on reverse if necessary and identify by block number) Transonic Flows Three Dimensional Flux-Split Algorithm Implicit → Navier-Stokes Equations Numerical Computations Asymmetric Shocks Composite Grid Scheme			
19. ABSTRACT (Continue on reverse if necessary and identify by block number)  The three dimensional flows over a projectile have been computed using an implicit, approximately factored, partially flux-split algorithm. A simple composite grid scheme has been developed in which a single grid is partitioned into a series of smaller grids for application which require an external large memory device such as the SSD of the CRAY X-MP/48 or multi-tasking. The accuracy and stability of the composite grid scheme has been tested by numerically simulating the flow over an ellipsoid at angle of attack and comparing the solution with a single grid solution. The flow field over a projectile at M = 0.96, 1.1 and 4° angle of attack has been computed using a fine grid and compared with experiment. [REDACTED]					
20. DISTRIBUTION/AVAILABILITY OF ABSTRACT <input checked="" type="checkbox"/> UNCLASSIFIED/UNLIMITED <input type="checkbox"/> SAME AS RPT <input type="checkbox"/> DTIC USERS			21. ABSTRACT SECURITY CLASSIFICATION UNCLASSIFIED		
22a. NAME OF RESPONSIBLE INDIVIDUAL JUBARAJ SAHU			22b. TELEPHONE (Include Area Code) (301) 278-3707	22c. OFFICE SYMBOL SLCBR-LF-R	

## TABLE OF CONTENTS

	<u>Page</u>
LIST OF FIGURE CAPTIONS.....	v
I. INTRODUCTION.....	1
II. NUMERICAL METHOD.....	2
1. GOVERNING EQUATIONS.....	2
2. IMPLICIT FINITE DIFFERENCE ALGORITHM.....	2
3. COMPOSITE GRID SCHEME.....	3
III. RESULTS.....	5
IV. CONCLUDING REMARKS.....	7
REFERENCES.....	25
DISTRIBUTION LIST.....	27

Accession For	
NTIS GRA&I	<input checked="" type="checkbox"/>
DTIC TAB	<input type="checkbox"/>
Unannounced	<input type="checkbox"/>
Justification	
By _____	
Distribution/	
Availability Codes	
Avail and/or	
Dist	Special
A-1	



LIST OF FIGURE CAPTIONS

<u>Figure</u>		<u>Page</u>
1	Single grid partitioned into smaller grids.....	8
2a	Surface grid for the Ellipsoid.....	9
2b	Longitudinal cross section of the computational grid.....	10
3	Surface pressure distribution, lee side, $M_{\infty} = 0.90$ and $\alpha = 10^\circ$ (first order accuracy at interfaces).....	11
4	Surface pressure distribution, lee side, $M_{\infty} = 0.90$ and $\alpha = 10^\circ$ (second order accuracy at interfaces).....	12
5	Model geometry of a projectile.....	13
6a	Computational grid (longitudinal cross section).....	14
6b	Computational grid (circumferential distribution).....	15
7	Pressure contours, $M_{\infty} = 0.96$ and $\alpha = 4^\circ$ .....	16
8	Mach contours, $M_{\infty} = 0.96$ and $\alpha = 4^\circ$ .....	17
9	Velocity vectors in the base region, $M_{\infty} = 0.96$ and $\alpha = 4^\circ$ .....	18
10	Longitudinal surface pressure distribution, wind side, $M_{\infty} = 0.96$ , $\alpha = 4^\circ$ .....	19
11	Longitudinal surface pressure distribution, lee side, $M_{\infty} = 0.96$ , $\alpha = 4^\circ$ .....	20
12	Circumferential surface pressure distribution, $M_{\infty} = 0.96$ , $\alpha = 4^\circ$ , $X/D = 5.19$ .....	21
13	Circumferential surface pressure distribution, $M_{\infty} = 0.96$ , $\alpha = 4^\circ$ , $X/D = 5.56$ .....	22
14	Longitudinal surface pressure distribution, wind side, $M_{\infty} = 1.1$ , $\alpha = 4^\circ$ .....	23
15	Longitudinal surface pressure distribution, lee side, $M_{\infty} = 1.1$ , $\alpha = 4^\circ$ .....	24

## I. INTRODUCTION

The transonic flow over bodies of revolution is of considerable interest in aerodynamics. The critical aerodynamic behavior occurs in this speed regime and a rapid increase in the aerodynamic coefficients is observed. The flowfield is complex due to the presence of shocks and can be characterized by strong viscous-inviscid, shock-boundary layer interactions. Further complications often occur in practical flows of interest due to the presence of separated flow regions which is especially true for flow at moderate to high angles of attack. As a result, it is desirable to use the Navier-Stokes computational technique to compute such flows.

In recent years Navier-Stokes<sup>1-3</sup> computational methods have been used to compute flow over bodies of revolution at transonic speeds. In Reference 1 the three dimensional flow over a boattailed afterbody was computed where the primary emphasis was on the boattail flow field. Calculations of three dimensional flow over a projectile have been made in Reference 2; however, the wake or base region flow was not computed. The wake region has been included in a three dimensional flowfield computation in Reference 3. These calculations were made with the compressible, thin-layer Navier-Stokes equations which were solved using the implicit Beam and Warming central finite difference scheme.<sup>4-6</sup> Generally, these calculations did not have sufficient grid resolution due to lack of adequate computer resources. With the advent of computers such as the CRAY X-MP/48 and CRAY 2 and the availability of the large memory (core memory of CRAY 2 and fast external memory device, SSD of the CRAY X-MP/48), it is now possible to use fine computational grids needed for three dimensional numerical simulation of transonic flows. Reference 7 is an excellent example where the CRAY 2 computer was used to perform transonic flow computations over a hemisphere cylinder at high angles of attack using its large incore memory. In the present work, we make extensive use of the SSD device of the CRAY X-MP/48 to provide sufficient grid resolution. This necessitates splitting the data base of a large single grid into smaller pieces that fit within the incore memory of the X-MP/48. While this break up can be achieved in various ways, the simplest approach is to break the single grid into a number of smaller grids.

The numerical scheme used is an implicit scheme based on flux-splitting<sup>8</sup> and upwind spatial differencing in the streamwise direction. Upwind schemes can have several advantages over central difference schemes, including natural numerical dissipation and better stability properties.

The accuracy of the composite grid scheme has been tested by numerically simulating the transonic flow over an ellipsoid at 10° angle of attack and comparing this result with the result obtained with a single grid. In addition, the flow over a secant-ogive-cylinder-boattail projectile has been computed using a fine grid at  $M = 0.96, 1.1$  and 4° angle of attack. These computed results have been compared with experimental data to determine the accuracy of the numerical predictions. In Section II, the governing equations, numerical procedure as well as the composite grid scheme have been described. Results are presented in Section III.

## II. NUMERICAL METHOD

### 1. GOVERNING EQUATIONS

The three dimensional Navier-Stokes conservation equations of mass, momentum, and energy can be represented in flux vector form as:

$$\partial_{\tau} \hat{Q} + \partial_{\xi} (\hat{F} + \hat{F}_v) + \partial_n (\hat{G} + \hat{G}_v) + \partial_{\zeta} (\hat{H} + \hat{H}_v) = 0 \quad (1)$$

where the independent variable  $\tau$  is the time and the spatial variables  $\xi, n, \zeta$  are chosen to map a curvilinear body conforming discretization into a uniform computational space. Here  $\hat{Q}$  contains all the dependent variables and  $\hat{F}$ ,  $\hat{G}$  and  $\hat{H}$  are the inviscid fluxes. The flux terms  $\hat{F}_v, \hat{G}_v$  and  $\hat{H}_v$  contain viscous derivatives and throughout a nondimensional form of the equations is used. The conservative form of the equations is maintained chiefly to capture the Rankine Hugoniot shock jump relations as accurately as possible.

For body conforming coordinates and high Reynolds number flow, if  $\zeta$  is the coordinate away from the surface, the thin layer approximation can be made in the  $\zeta$  direction and the governing equations can be written as:

$$\partial_{\tau} \hat{Q} + \partial_{\xi} \hat{F} + \partial_n \hat{G} + \partial_{\zeta} \hat{H} = Re^{-1} \partial_{\zeta} \hat{S}. \quad (2)$$

Here the viscous terms in  $\zeta$  have been collected into the vector  $\hat{S}$  and the nondimensional reciprocal Reynolds number is extracted to indicate a viscous flux term.

In differencing these equations it is often advantageous to difference about a known base solution denoted by subscript 0 as:

$$\begin{aligned} \delta_{\tau} (\hat{Q} - \hat{Q}_0) + \delta_{\xi} (\hat{F} - \hat{F}_0) + \delta_n (\hat{G} - \hat{G}_0) + \delta_{\zeta} (\hat{H} - \hat{H}_0) - Re^{-1} \delta_{\zeta} (\hat{S} - \hat{S}_0) \\ = -\partial_{\tau} \hat{Q}_0 - \partial_{\xi} \hat{F}_0 - \partial_n \hat{G}_0 - \partial_{\zeta} \hat{H}_0 + Re^{-1} \partial_{\zeta} \hat{S}_0 \end{aligned} \quad (3)$$

where  $\delta$  indicates a general difference operator, and  $\partial$  is the differential operator. If the base state can be properly chosen, the differenced quantities can have smaller and smoother variation and therefore less differencing error. The freestream is used as a base solution in the present formulation.

### 2. IMPLICIT FINITE DIFFERENCE ALGORITHM

The implicit approximately factored scheme for the thin layer Navier-Stokes equations that uses central differencing in the  $n$  and  $\zeta$  directions and upwinding in  $\xi$  is written in the form:

$$\begin{aligned}
& [I + h\delta_{\xi}^b(\hat{A}^+)^n + h\delta_{\xi}\hat{C}^n - hRe^{-1}\bar{\delta}_{\xi}J^{-1}\hat{M}^nJ - D_i|_{\xi}] \\
& \times [I + h\delta_{\xi}^f(\hat{A}^-)^n + h\delta_n\hat{B}^n - D_i|_n]\Delta Q^n = \\
& -\Delta t\{\delta_{\xi}^b[(\hat{F}^+)^n - \hat{F}_{\infty}^+] + \delta_{\xi}^f[(\hat{F}^-)^n - \hat{F}_{\infty}^-] + \delta_n(\hat{G}^n - \hat{G}_{\infty}) \\
& + \delta_{\xi}(\hat{H}^n - \hat{H}_{\infty}) - Re^{-1}\bar{\delta}_{\xi}(\hat{S}^n - \hat{S}_{\infty})\} - D_e(\hat{Q}^n - \hat{Q}_{\infty})
\end{aligned} \tag{4}$$

where  $h = \Delta t$  or  $(\Delta t)/2$  and the freestream base solution is used. Here  $\delta$  is typically a three point second order accurate central difference operator,  $\bar{\delta}$  is the midpoint operator used with the viscous terms, and the operators  $\delta_{\xi}^b$  and  $\delta_{\xi}^f$  are backward and forward three-point difference operators. The flux  $F$  has been split into  $\hat{F}^+$  and  $\hat{F}^-$ , according to its eigenvalues and the matrices  $\hat{A}, \hat{B}, \hat{C}$  and  $\hat{M}$  result from local linearization of the fluxes about the previous time level. Here  $J$  denotes the Jacobian of the coordinate transformation. Dissipation operators,  $D_e$  and  $D_i$  are used in the central space differencing directions.<sup>7</sup>

The factored left hand side operators can be readily inverted by sweeping and inversion of tridiagonal matrices with  $5 \times 5$  blocks. This two factor implicit scheme is readily vectorized or multi-tasked in planes of  $\xi =$  constant.

### 3. COMPOSITE GRID SCHEME

In the present work, a composite grid scheme has been developed in which a large single grid is split into a number of smaller grids so that each of these grids can use, in turn, the available core memory while the rest are stored on the SSD device. The use of such composite scheme however, requires special care in storing and fetching the interface boundary data.

If a code is well-written in a modular form for a single grid, it is a relatively simple task to reconfigure it either as a composite grid code, or a blocked grid data structure code using an external large memory device such as the SSD of the CRAY X-MP/48. The simplest case to begin with is the blocked grid data structure code in which a single large grid is partitioned into a series of smaller grid blocks as sketched in Figure 1. Such a partitioning of a single original grid may come about because all of the single grid will not fit into a particular computer's high speed memory or because a block iterative technique is in use. To make a code work for a partitioned grid that works for a single grid it is necessary to build an external data management scheme for a block update process (e.g. block iterative or block time dependent process). In a block update scheme, if data from one subgrid is used to

update the interface boundary of another subgrid, the subblock solution will approach the solution of the single grid. (We say approach because the differencing approximations near a boundary may drop in order of accuracy or use metrics evaluated in a different manner. Likewise, iterative convergence may be less tight in a given block.)

A code developed for a single grid can be made to work for a block grid structure by: 1) mapping and storing the information for each grid onto a large memory; and 2) supplying interface boundary arrays, pointers and updating procedures. Consider the situation in Figure 1 in which the single grid from  $J = 1, J_{\max}$  is partitioned into three grids. Although not shown in this figure, the base region of the projectile is easily included by adding one or more zones in that region. We begin the procedure with grid G1. For each grid, an estimated solution (or initial guess) is put into the large memory along with all pertinent information such as the grid, metrics,  $M_\infty$ ,  $R_e$  etc. This data is brought into the working memory and appropriate boundary update information is also called in and used to update any interface boundaries. At this point, the problem of dealing with a single grid code must be dealt with. Solution variables are updated as before (more than one iterative update per subgrid is possible or interface boundaries can be iteratively corrected). The updated solution is then stored back into large (external) memory. Also stored into the appropriate locations is any information needed to update other interface boundaries. This procedure is repeated in the next subgrid and so on.

The chief complexity of any blocked or composite grid scheme is the problem of storing and fetching the interface boundary data from its appropriate place, i.e., setting up the proper bookkeeping. Additional complications come about when we try to make blocked grids with interface boundaries give a solution which is identical to the solution obtained by a large single grid with no interface boundaries. This involves maintaining the same or equivalently good metrics, differencing accuracy, and conservation statements etc., at or near interface boundaries which would exist on a continuous smooth grid. One choice that allowed a simpler management of the interface boundary data while still maintaining second order accuracy was to use central finite differences at these boundaries. As will be shown in the results, this procedure works rather well compared to dropping the accuracy of the upwind scheme from second order to first order.

For the simple partitioning shown in Figure 1, all subgrid points are members of the original grid and no interpolations are required. This procedure thus, has the advantage over patched or overset grid schemes which do require interpolations. The partitioned grid has four interface boundaries,  $J_1 = J_{1\max}$ ,  $J_2 = 1$ ,  $J_2 = J_{2\max}$  and  $J_3 = 1$ . Data for these planes are to be supplied from the other grids by injecting interior values of the other grid onto the interface boundaries. For example, the  $J_1 = J_{1\max}$  boundary of G1 may be taken as the  $J_2 = 2$  or the  $J_2 = 3$  plane interior values of G2. More overlap would mean more implicit like behavior. Because only one grid and some boundary and pointer arrays can be in the working memory at one time, a low storage scheme to shuffle data from one grid to another must be used. In working on grid G1 all of the usual data  $Q, x, y, z, \dots$  of grid G1 plus the

interface boundary data stored in an array, say, QB from grid G2,G3,... will have to be in working memory. The array QB need only store Q on the interface boundary as other data such as metrics on the interface boundary can be computed from the usual data x,y,z... After updating grid G1, interface boundary data QB supplied by G1 for the other grids should be loaded while all data of G1 is still in memory. Thus the data array QB should be shuffled back into a permanent large external memory, say QBC, in such a way that it can be readily brought back for grid G2, grid G3, etc. There are several ways to store QB in memory, the approach selected here is flexible and is used in the Chimera code.<sup>9</sup>

### III. RESULTS

The implicit time marching procedure was used to obtain the desired steady state result starting from initial freestream conditions everywhere. Boundary conditions were updated explicitly at each time step. The solution residual dropped at least three orders of magnitude before converged solutions were obtained. In addition, the surface pressure distribution was checked for time invariance. Solutions have been obtained for two cases: (i) flow over an ellipsoid at  $M_\infty = 0.90$  and  $\alpha = 10^\circ$ , primarily to check the accuracy of the composite grid solution and (ii) flow over a projectile at  $M_\infty = 0.96, 1.1$  and  $\alpha = 4^\circ$  which is calculated using a fine grid.

First, the flow over an ellipsoid at  $M_\infty = 0.90$  and  $10^\circ$  angle of attack is considered. Figure 2 shows the computational grid for the ellipsoid. Figure 2a shows the surface of the ellipsoid while Figure 2b is a cross-section of the full grid showing the longitudinal grid point distribution. This grid has 41 points in the streamwise direction, 18 points in the circumferential, and 31 points in the normal direction. Such a small grid was chosen so that the full grid solution could be obtained using a CRAY X-MP/48 with a two million word central core memory. The full grid was then partitioned into three smaller grids and the SSD device was used to obtain the solution for this composite grid scheme. Figure 3 shows the surface pressure distribution in the lee side. Here, the full grid solution is shown as a solid line and the composite grid solution as a dotted line. The differences in these curves are apparent and occur near  $X = .3$  and  $.8$  at the interfaces between the partitioned grids. The spatial accuracy at the interface was first order in this case. Improving the spatial differencing accuracy at these boundaries to second order resulted in the solution shown in Figure 4. As shown in this figure, the composite grid solution is virtually identical to the full grid solution.

Second, the flow over a projectile at a transonic speed  $M_\infty = 0.96$  and at a higher transonic speed  $M_\infty = 1.1$  for  $\alpha = 4^\circ$  was computed. The model used for the experiment and computational study presented here is an idealization of a realistic artillery projectile geometry. The experimental model shown in Figure 5 consists of a three-caliber (one-caliber = maximum body diameter), sharp, secant-ogive nose, a two-caliber cylindrical mid-section and a one-caliber  $7^\circ$  conical afterbody or boattail. A similar model was used for the computational studies with the only difference being a 5% rounding of the nose tip. The nose tip rounding was done for computational efficiency and is considered to have little impact on the final integrated forces.

Experimental pressure data<sup>10-11</sup> are available for this shape and were obtained in the NASA Langley eight foot Pressure Tunnel using a sting mounted model. The test conditions of 1 atm supply pressure and 320 K supply temperature resulted in a Reynolds number of  $4.5 \times 10^6$  based on model length.

The computational grid used for this computation is shown in Figure 6. Figure 6a shows the longitudinal cross section of the 3D grid while Figure 6b shows the circumferential distribution of grid points. As shown in Figure 6a, the clustering of grid points near the body surface is done to resolve the viscous boundary layer near the body surface. Grid clustering has also been used in the longitudinal direction near the boattail and the base corners where large gradients in the flow variables are expected. The grid consists of 162 points in the streamwise direction, 36 points in the circumferential direction and 50 points in the normal direction. This amounts to a little over 12 million words of storage for the code on the CRAY X-MP/48. Only up to 4 Mw of central core memory was easily accessible; therefore, the full grid was partitioned into four smaller grids each of which would use the core memory in turn while the rest is stored on the SSD device. In addition, the grid is made to wrap around the base corner to facilitate the generation of the large single grid. What affect it has on the base region flow is currently under investigation and has not been studied here. The primary emphasis in this research was on the use of the composite grid technique itself. The computations were performed on the CRAY X-MP/48 at the US Army Ballistic Research Laboratory.

For the computation of turbulent flow, a turbulence model must be supplied. In the present calculation, a two layer algebraic eddy viscosity model due to Baldwin and Lomax<sup>12</sup> is used. Figure 7 and 8 show the pressure contours and Mach contours for the projectile in the windward and leeward planes. As shown in Figure 7, the pressure contours show the expansions at the ogive-cylinder, boattail and base corners. The expansions at the base corners are rather weak. This figure also indicates the presence of shock waves on the cylinder and also on the boattail. Figure 8 shows the Mach number contours. It clearly shows the expansions and shock structure that typically occur on the projectile at transonic speeds. Sharp shocks are clearly observed on the boattailed flow field which are also asymmetrically located (the one on the wind side being closer to the base than its counterpart on the lee side.) This figure also indicates the presence of strong free shear layers in the base region flow field and also shows the expected asymmetric flow pattern in the wake. The asymmetric wake flow can be better seen in Figure 9 which shows the velocity field in the near wake for both the wind as well as the leeside. The recirculatory flow pattern in the base region is evident. Three pairs of separated flow bubbles can be clearly seen in this figure. Each pair consists of two vortices, one clockwise and one counter-clockwise. Two of these pairs occur in the leeside whereas only one pair can be seen in the windside. The experimental model was sting mounted in the base region and current work is in progress to model the sting before accuracy of the base region flow prediction can be determined. In the present computation, the sting has not been modeled.

Figure 10 shows the surface pressure distribution as a function of the longitudinal position for the wind side. The computed result is compared with experimental data<sup>10</sup> shown in circles and is in very good agreement. The expansions and recompressions near the ogive-cylinder and cylinder-boattail

junctions are captured adequately by the computations. Comparison of the surface pressure on the lee side is shown in Figure 11. A small discrepancy can be seen on the cylinder and boattail sections. The computed result, however, is generally in good agreement with the experimental data. Figures 12 and 13 show the circumferential surface pressure distributions for longitudinal positions  $X/D = 5.19$  and  $5.56$ , respectively. Both of these longitudinal positions are on the boattail. In these figures, the present computed result is compared with experimental data shown in circles and also with a previous computational result obtained on a rather coarse mesh.<sup>3</sup> Apart from the small discrepancy near the lee side ( $\phi = 180^\circ$ ), the present computed result is in good agreement with experimental data and is more accurate compared to the previous computed result (see Figure 12). The agreement of the present result with experiment is very good near the wind side ( $\phi = 0$ ). Figure 13 shows the circumferential surface pressure comparison at a longitudinal position  $X/D = 5.56$ . As shown in this figure, the present numerical result is in excellent agreement with the experimental data. The improved accuracy of the present numerical solution compared with the previous coarse grid solution is obvious.

Numerical solution has also been obtained at a high transonic speed  $M_\infty = 1.1$  and  $\alpha = 4^\circ$ . Comparisons of the longitudinal surface pressure distributions for both wind side and lee side have been made with experimental data<sup>10</sup> and are shown in Figures 14 and 15. The agreement of the computed surface pressures with experiment is very good. At this high transonic Mach number, the shocks on the cylinder as well as on the boattail are very weak as evidenced by the absence of sharp rise in pressure in those areas. Strong shock waves occur at lower transonic Mach numbers, for example at  $M_\infty = 0.96$  and  $\alpha = 4^\circ$  (see Figure 10). The expansions and recompressions near the ogive-cylinder and cylinder-boattail junctions can be clearly observed in Figures 14 and 15.

#### IV. CONCLUDING REMARKS

In conjunction with a new Navier-Stokes code, a simple composite grid scheme has been developed which allows fine computational grids needed for accurate transonic flow computations to be obtained on a CRAY X-MP/48 computer. The numerical method uses an implicit, approximately factored, partially upwind (flux-split) algorithm.

The accuracy and stability of the composite grid scheme have been tested by numerically simulating the flow over an ellipsoid at angle of attack ( $M = 0.90$ ,  $\alpha = 10^\circ$ ) and comparing this solution with a single grid solution. The flow fields over a projectile at  $M_\infty = 0.96$ ,  $1.1$  and  $\alpha = 4^\circ$  have been computed using a fine grid and compared to experiment. The computed surface pressures are in very good agreement with experimental data. Currently work is in progress to analyze and determine the accuracy of the wake region flow and also to determine the critical aerodynamic behavior at transonic speeds.

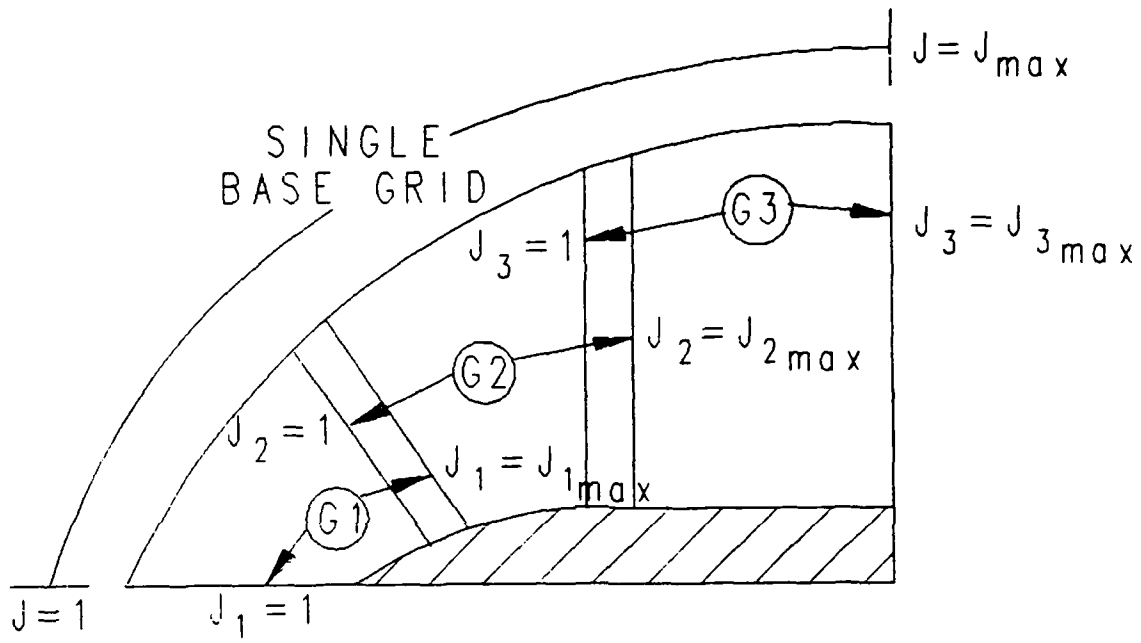


Figure 1. Single grid partitioned into smaller grids.

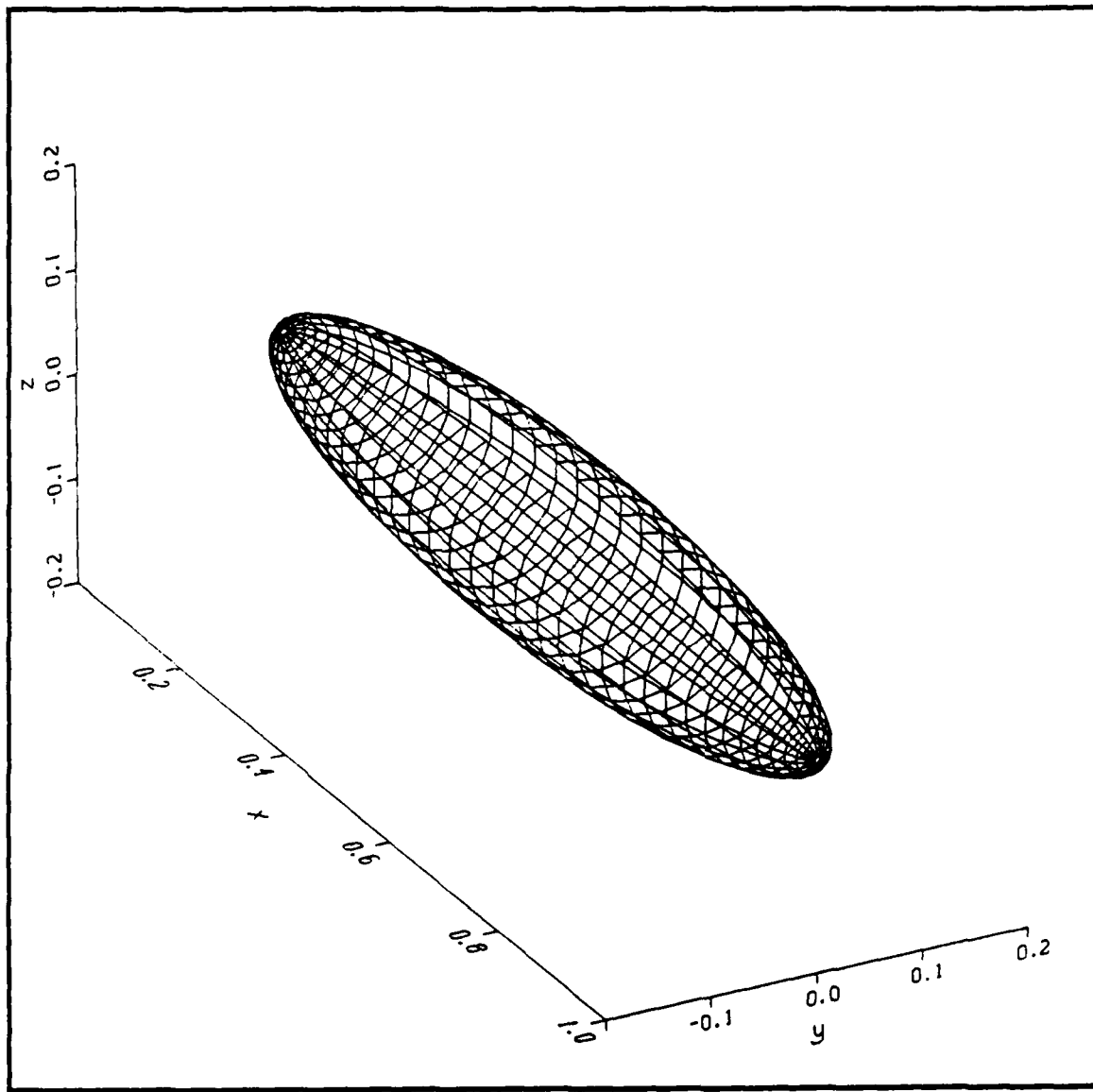


Figure 2a. Surface grid for the Ellipsoid.

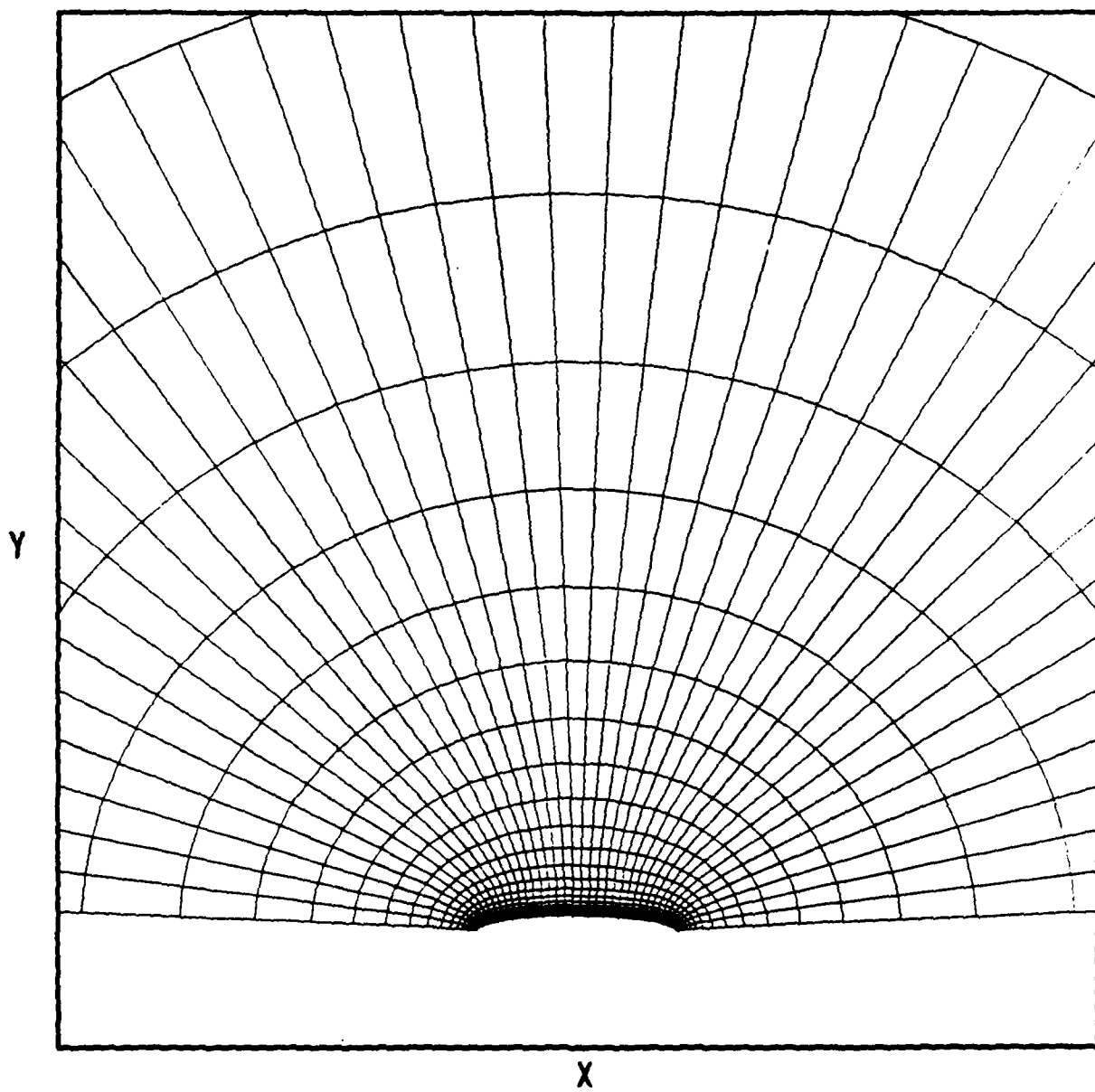


Figure 2b. Longitudinal cross section of the computational grid.

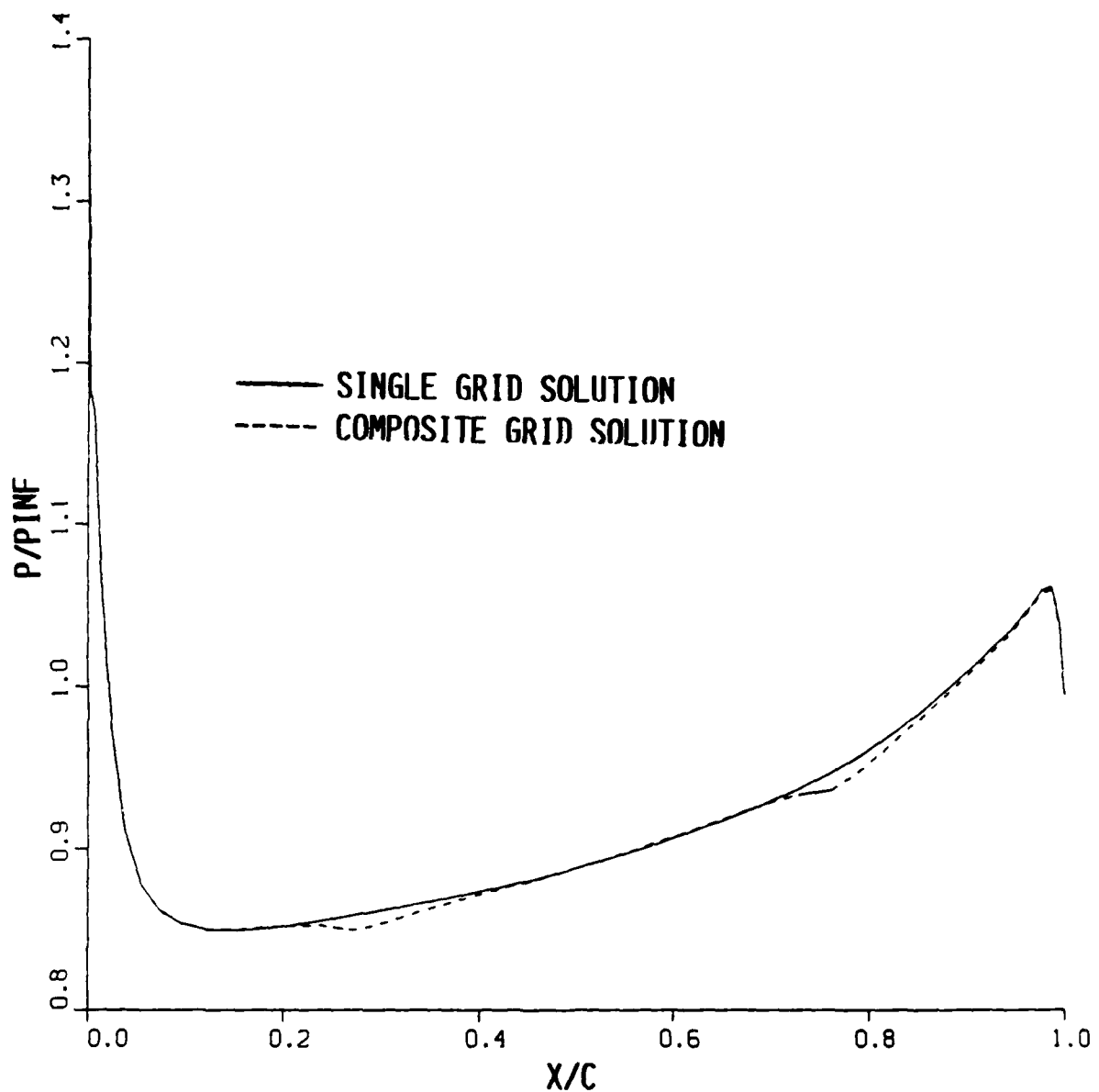


Figure 3. Surface pressure distribution, lee side,  $M_{\infty} = 0.90$  and  $\alpha = 10^\circ$   
(first order accuracy at interfaces).

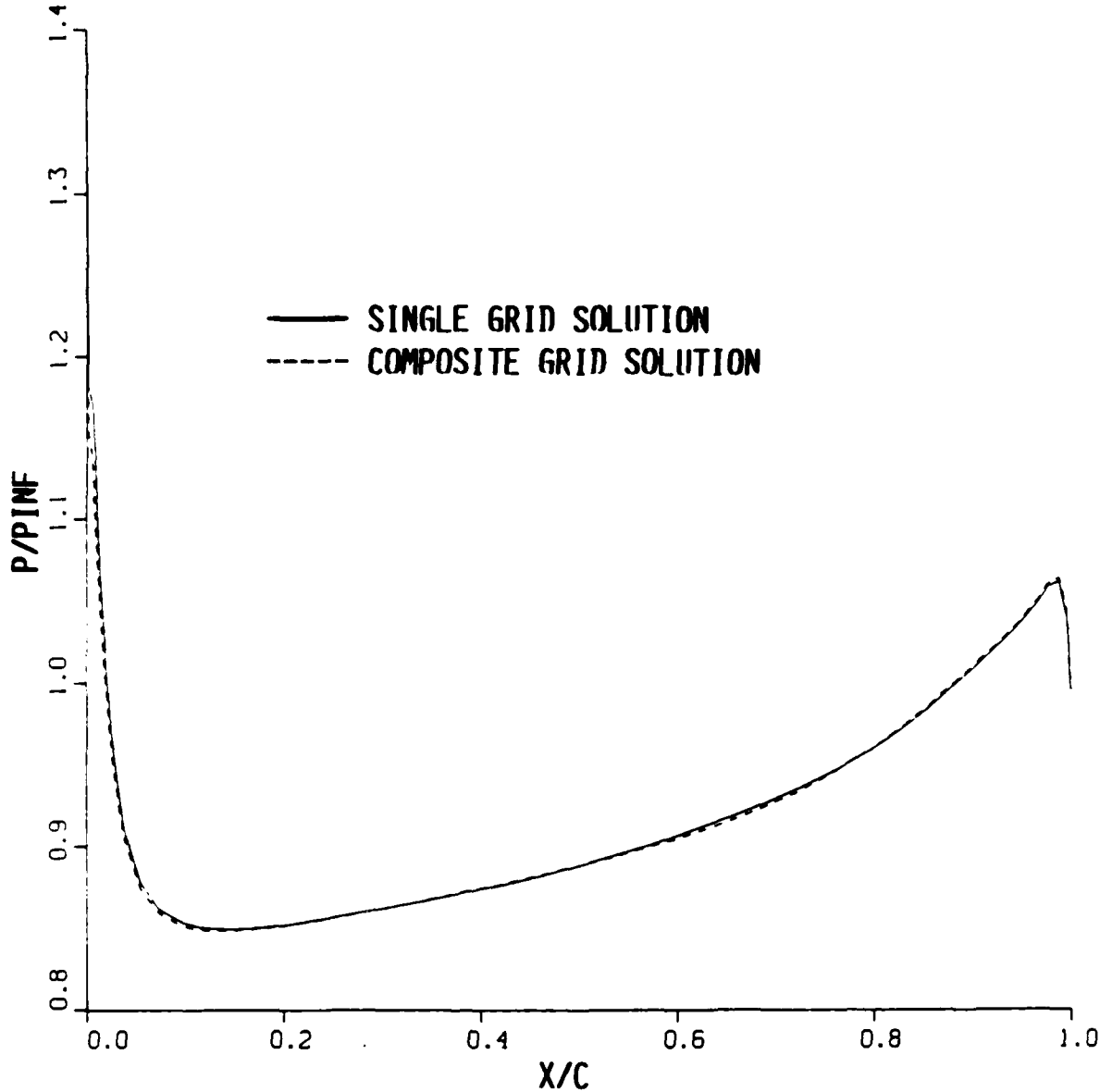


Figure 4. Surface pressure distribution, lee side,  $M_{\infty} = 0.90$  and  $\alpha = 10^\circ$   
(second order accuracy at interfaces).

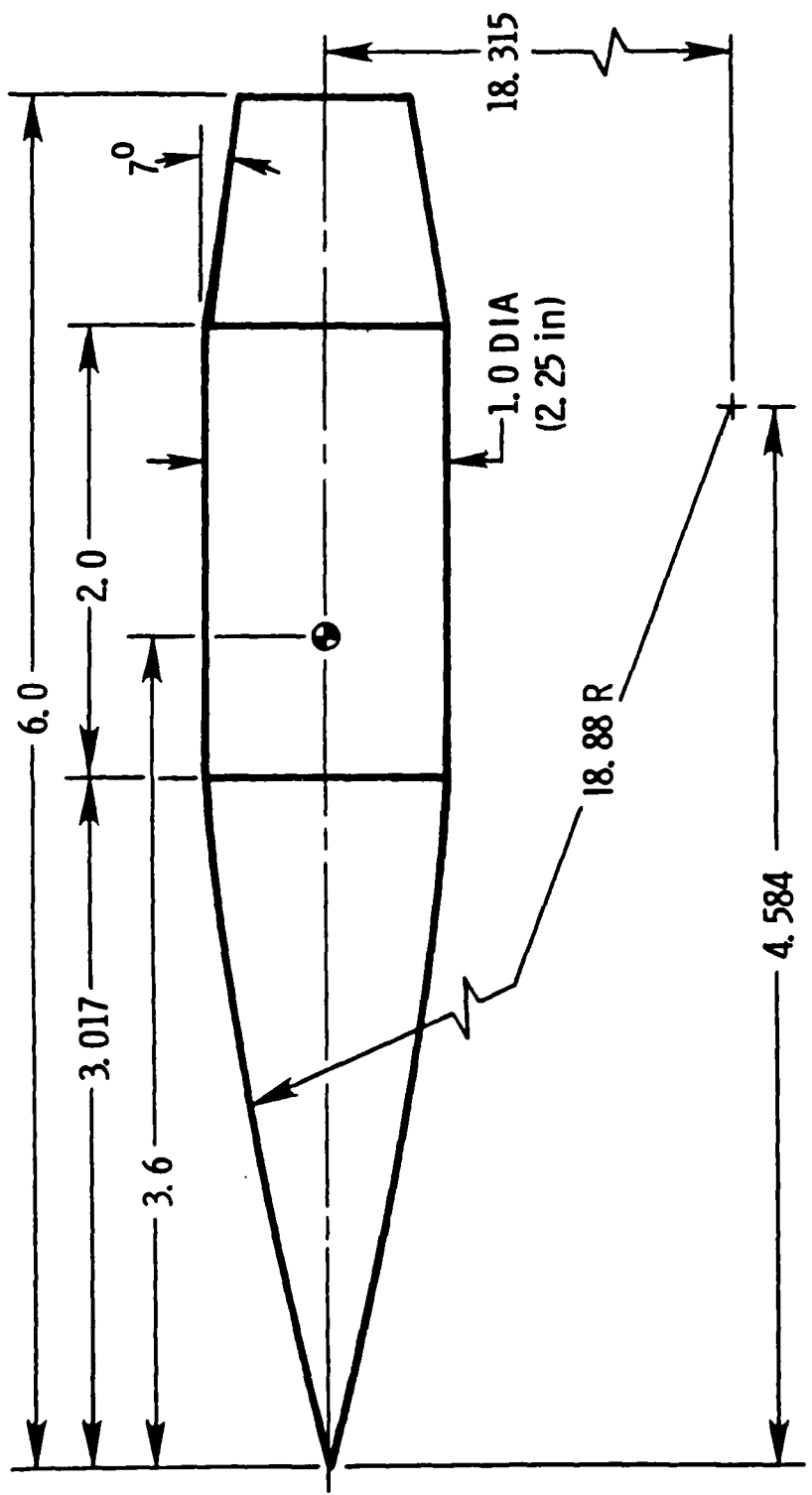


Figure 5. Model geometry of a projectile.

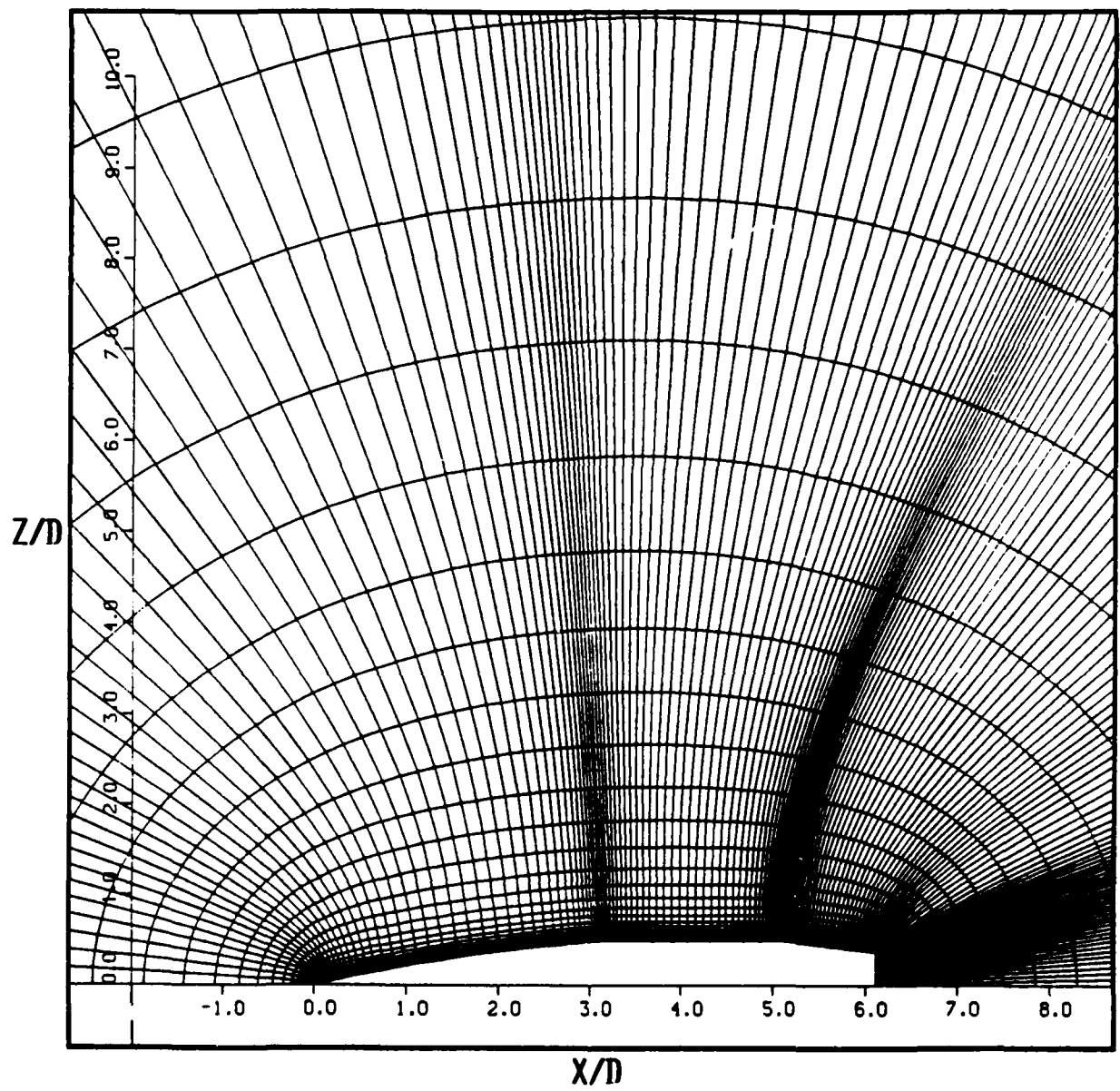


Figure 6a. Computational grid (longitudinal cross section).

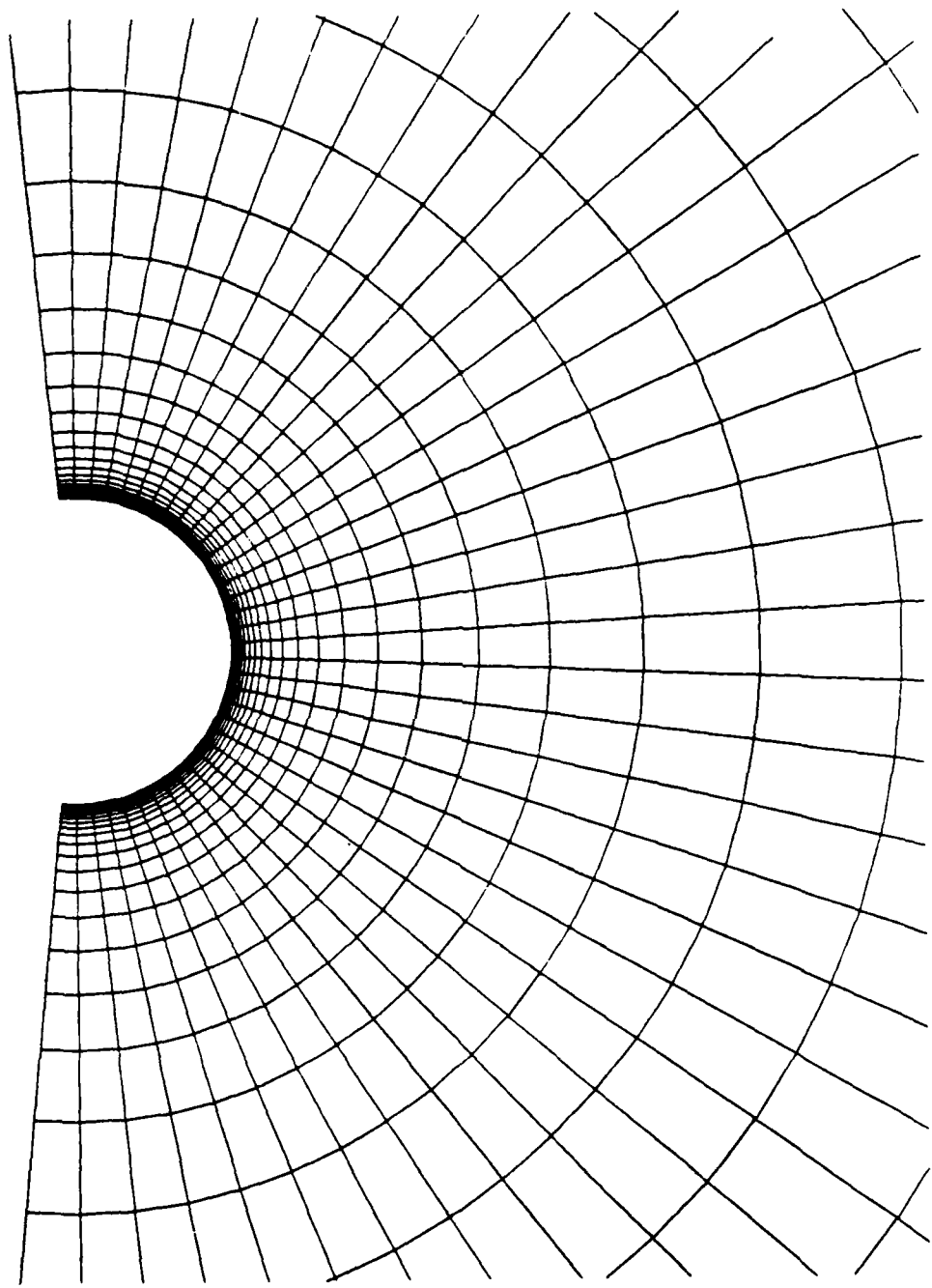


Figure 6b. Computational grid (circumferential distribution).

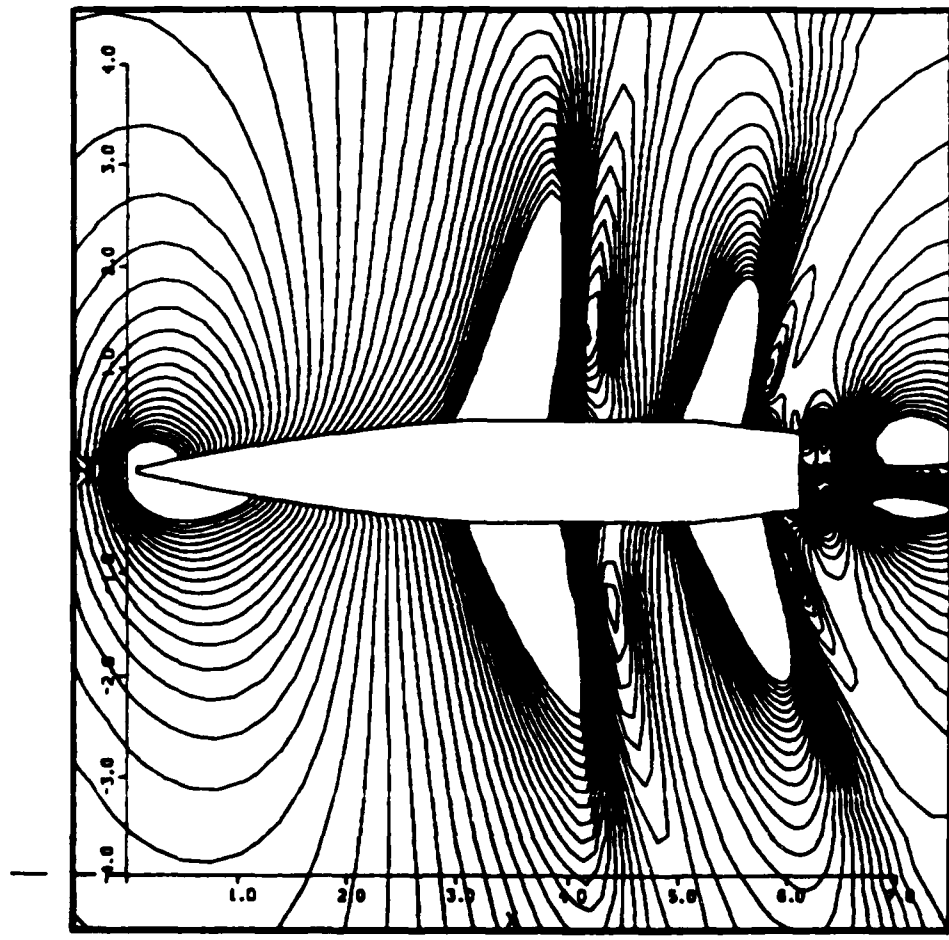


Figure 7. Pressure contours,  $M_{\infty} = 0.96$  and  $\alpha = 4^\circ$ .

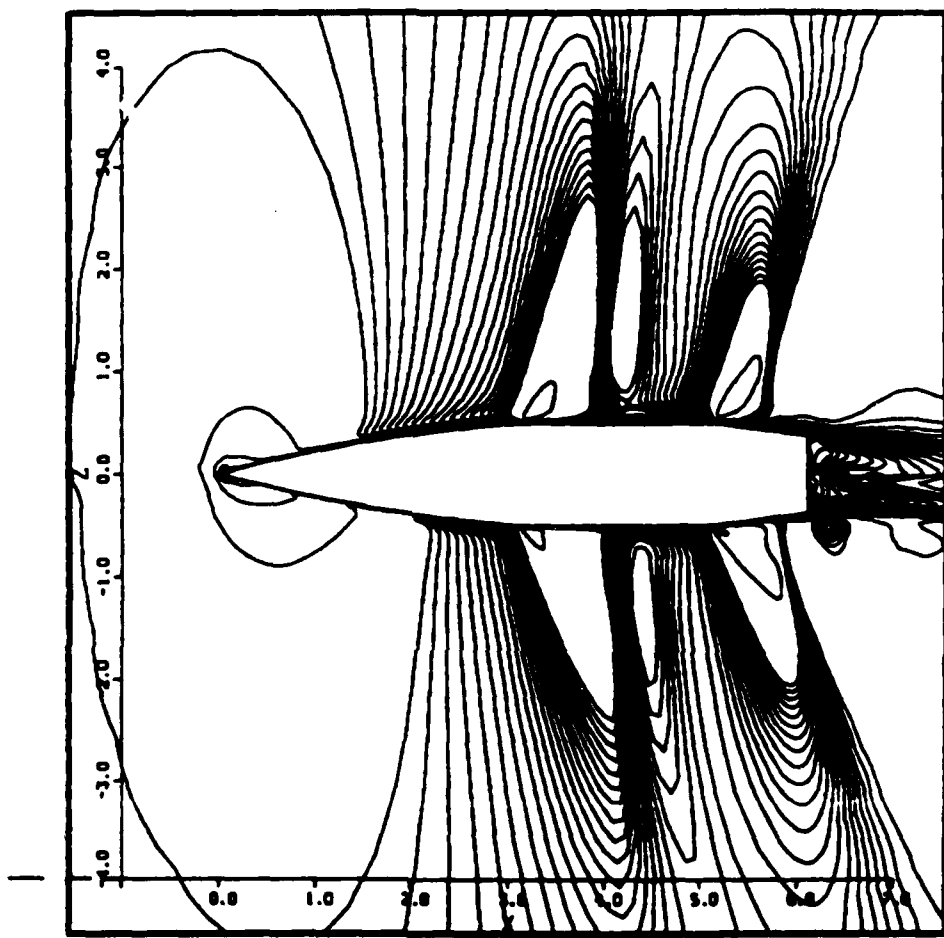


Figure 8. Mach contours,  $M_\infty = 0.96$  and  $\alpha = 4^\circ$ .

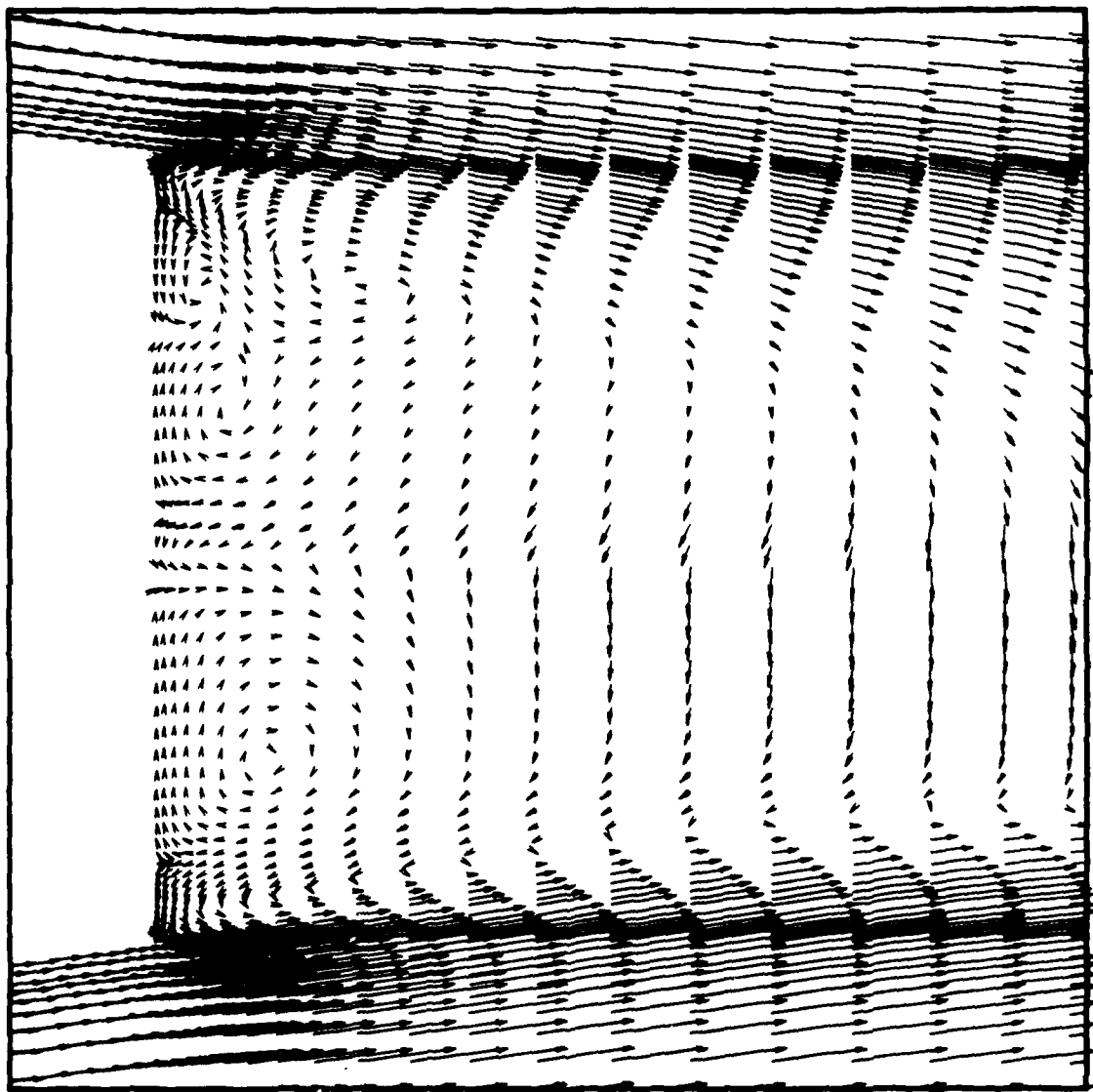


Figure 9. Velocity vectors in the base region,  $M_\infty = 0.96$  and  $\alpha = 4^\circ$ .

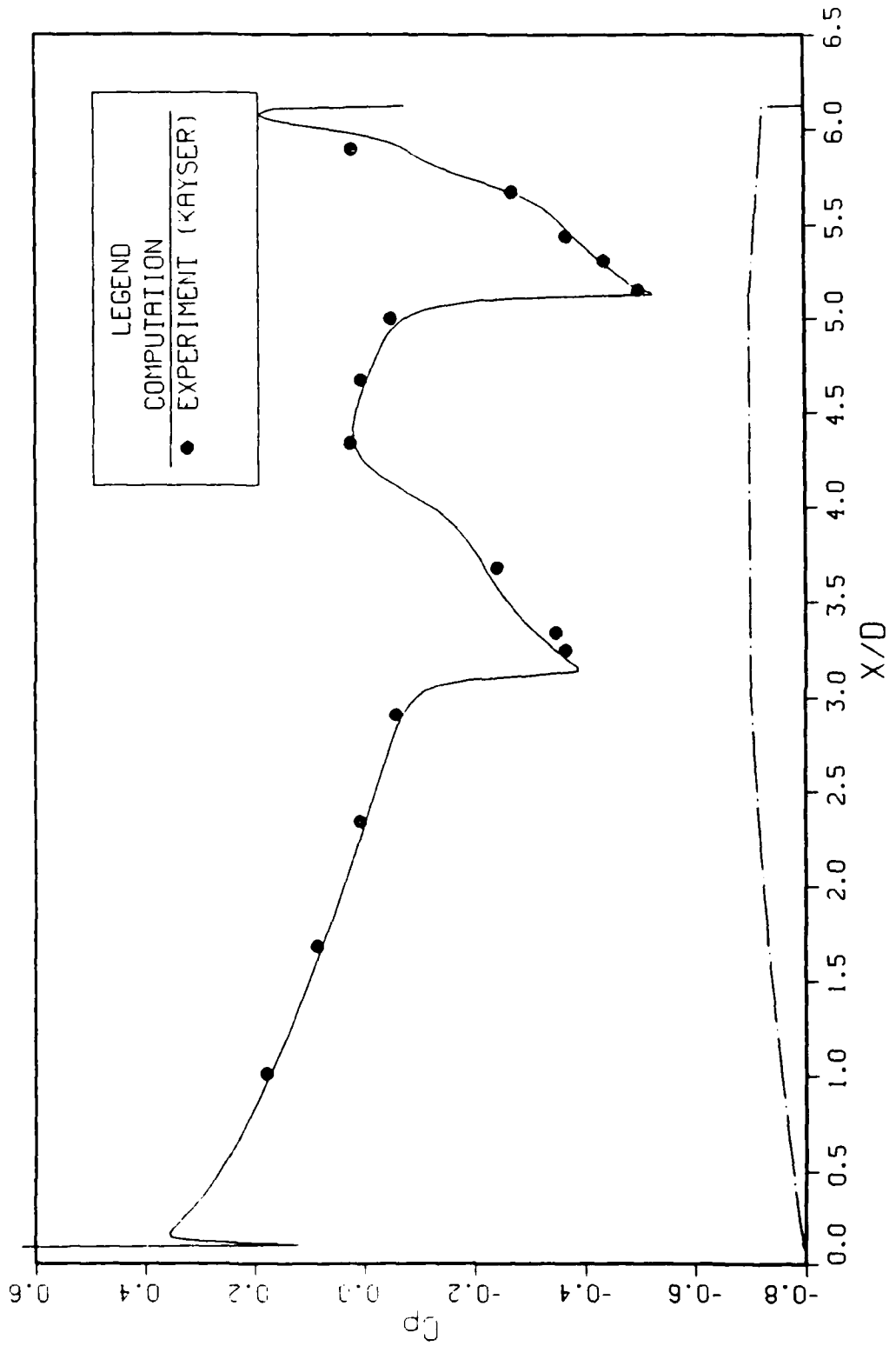


Figure 10. Longitudinal surface pressure distribution, wind side,  $M_\infty = 0.96$ ,  $\alpha = 4^\circ$ .

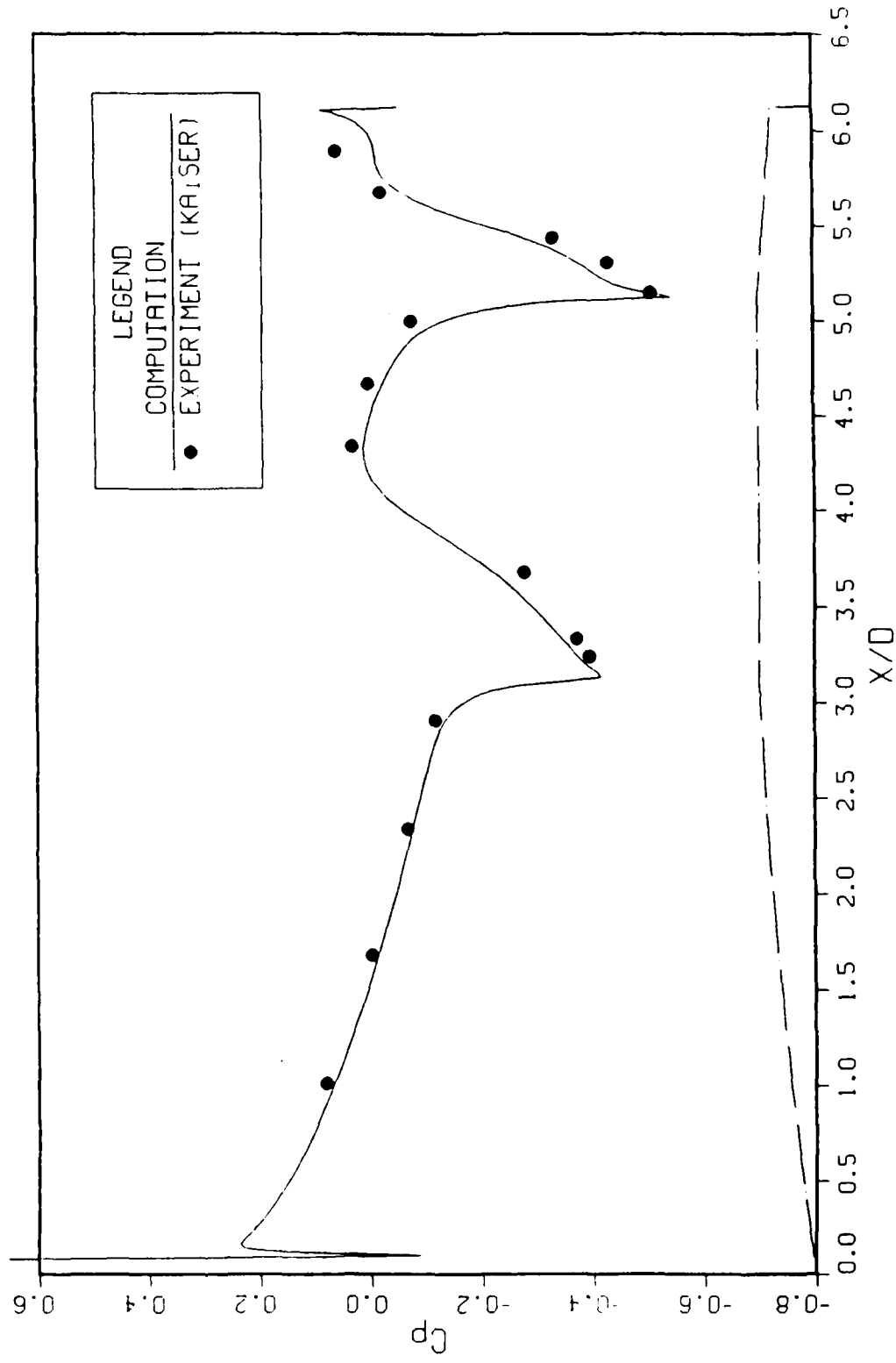


Figure 11. Longitudinal surface pressure distribution, lee side,  $M_\infty = 0.96$ ,  $\alpha = 4^\circ$ .

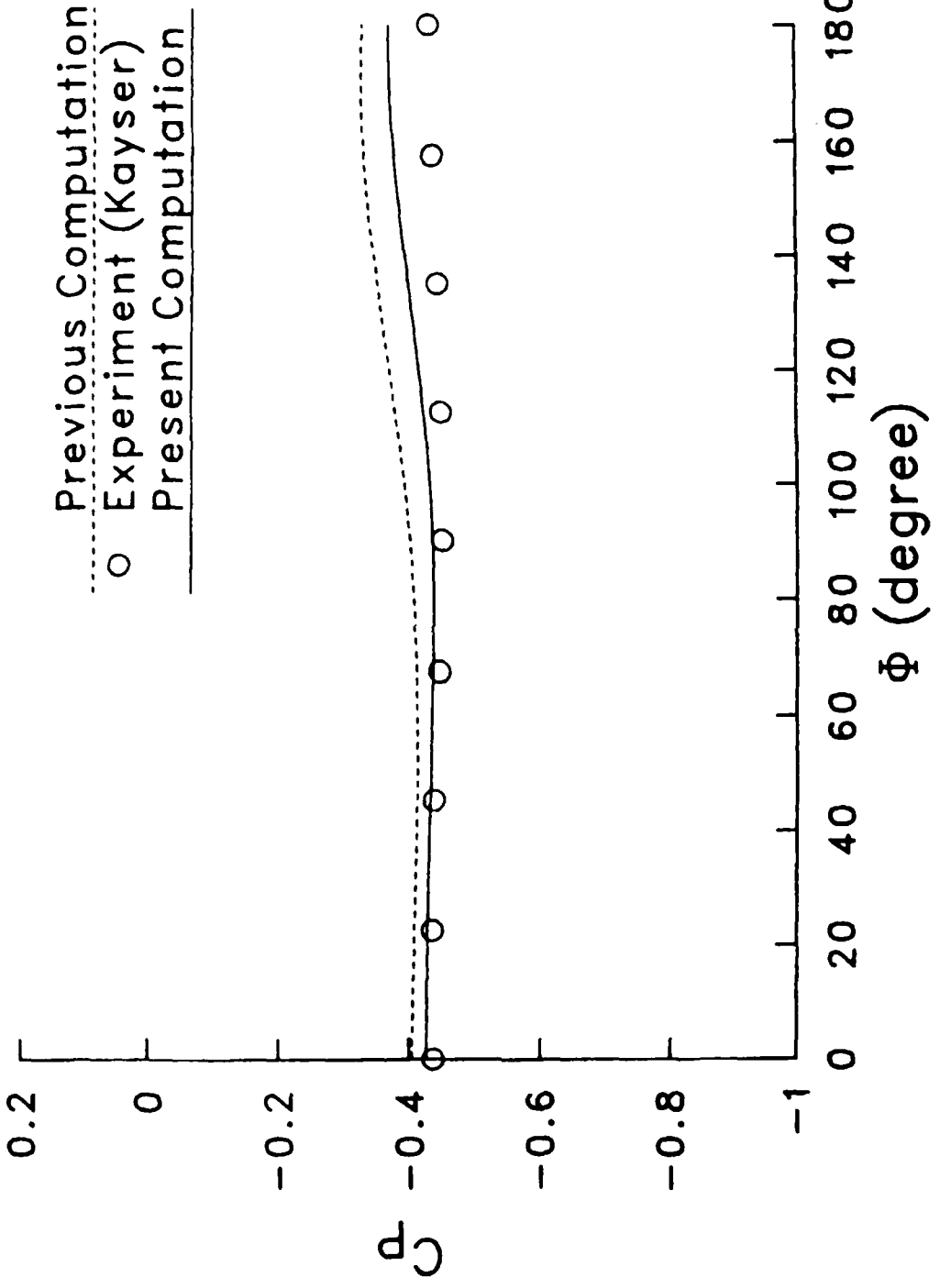


Figure 12. Circumferential surface pressure distribution,  $M_\infty = 0.96$ ,  $\alpha = 4^\circ$ ,  $X/D = 5.19$ .

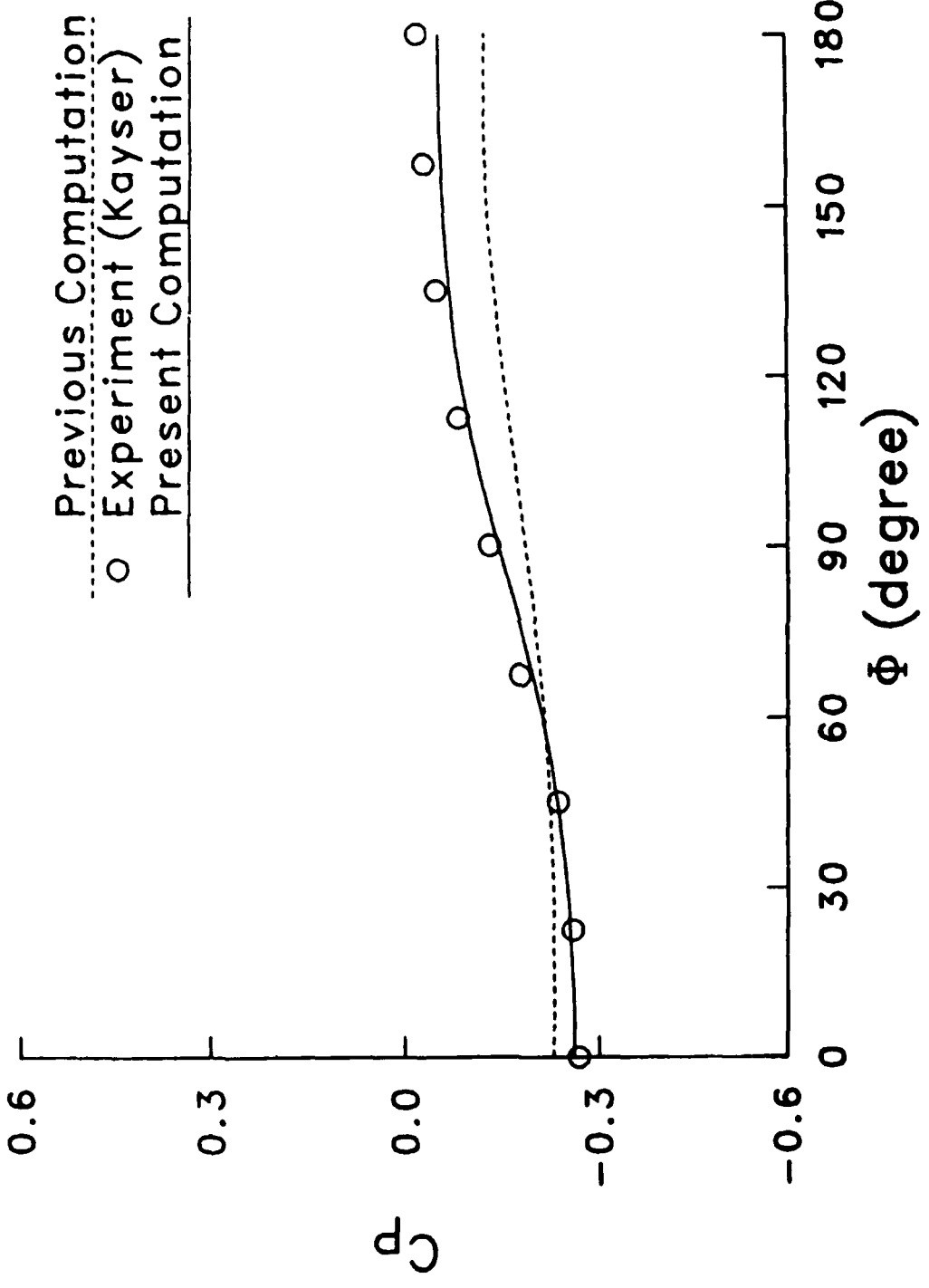


Figure 13. Circumferential surface pressure distribution,  $M_\infty = 0.96$ ,  $\alpha = 4^\circ$ ,  $X/D = 5.56$ .

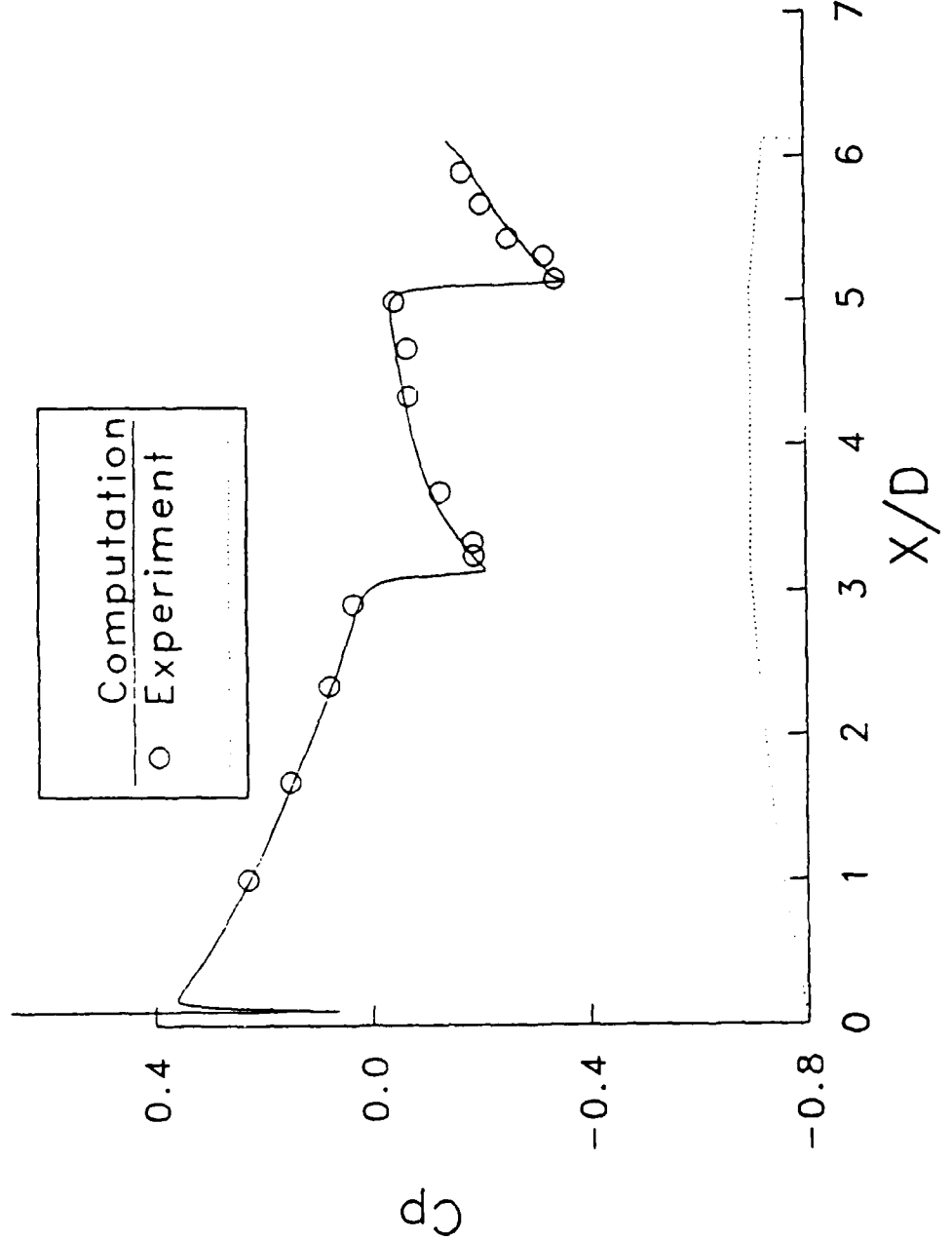


Figure 14. Longitudinal surface pressure distribution, wind side,  $M_\infty = 1.1$ ,  $\alpha = 4^\circ$ .

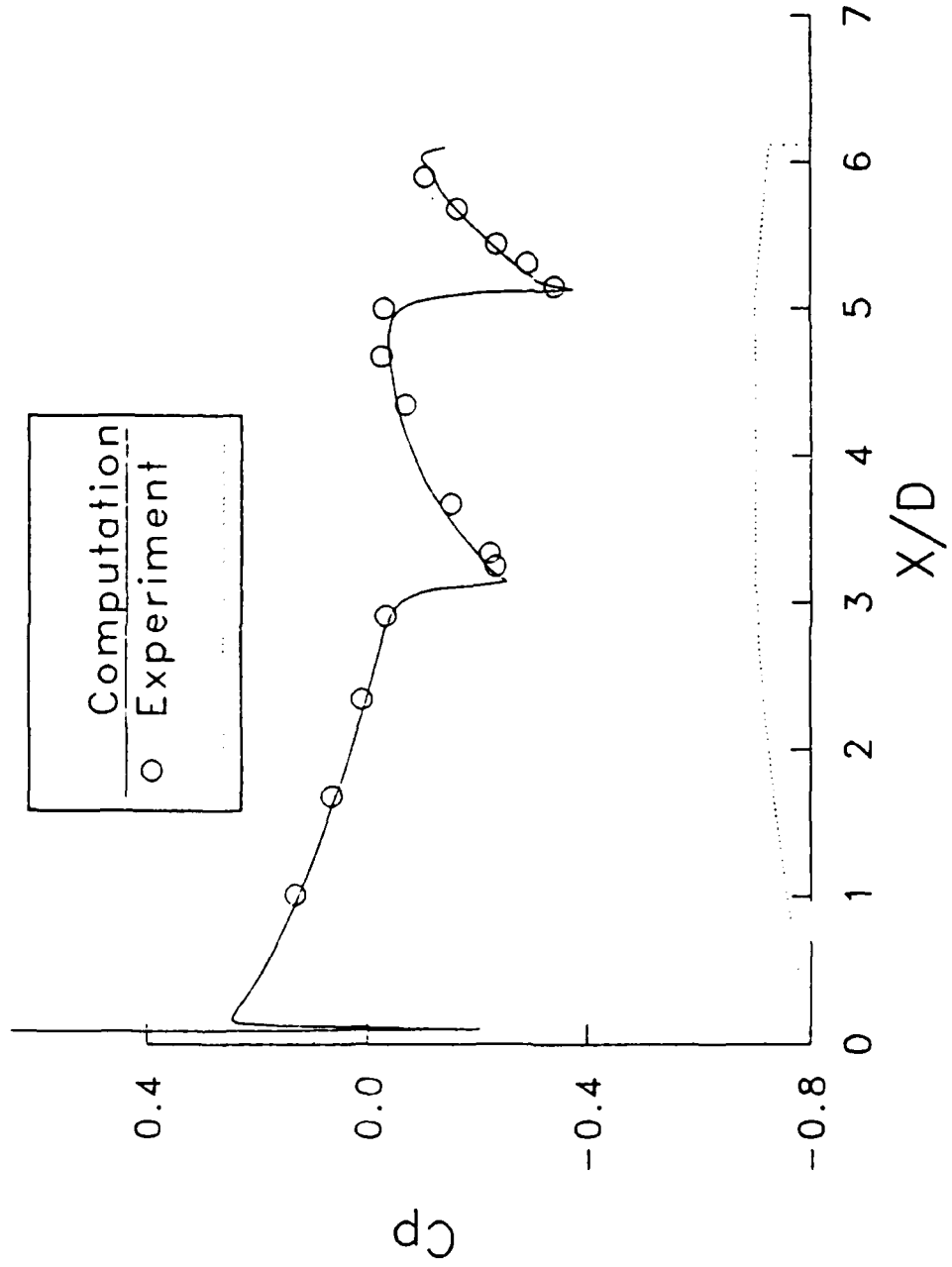


Figure 15. Longitudinal surface pressure distribution, lee side,  $M_\infty = 1.1$ ,  $\alpha = 4^\circ$ .

## REFERENCES

1. Deiwert, G.S., "Numerical Simulation of Three Dimensional Boattail Afterbody Flowfield," AIAA Journal, Vol. 19, May 1981.
2. Nietubicz, C.J. et al, "Computations of Projectiles Magnus Effect at Transonic Velocities, AIAA Journal, Vol. 23, No. 7, July 1985.
3. Sahu, J., "Three Dimensional Base Flow Calculation for a Projectile at Transonic Velocity," AIAA Paper No. 86-1051, May 1986.
4. Beam, R. and Warming, R.F., "An Implicit Factored Scheme for the Compressible Navier-Stokes Equations," AIAA Paper No. 85-1815-CP, August 1985.
5. Steger, J.L., "Implicit Finite Difference Simulation of Flow About Arbitrary Geometries with Application to Airfoils," AIAA Journal, Vol. 16, No. 4, July 1978, pp. 679-686.
6. Pulliam, T.H. and Steger, J.L., "On Implicit Finite-Difference Simulations of Three-Dimensional Flow, AIAA Journal, Vol. 18, No. 2, February 1980, pp. 159-167
7. Ying, S.X., Steger, J.L., Schiff, L.B. and Baganoff, D., Numerical Simulation of Unsteady, Viscous, High-Angle-of-Attack Flows Using a Partially Flux-Split Algorithm," AIAA Paper No. 86-2179, August 1986.
8. Steger, J.L. and Warming, R.F., "Flux Vector Splitting of the Inviscid Gasdynamic Equations with Application to Finite-Difference Methods," Journal of Computational Physics, Vol. 40, No. 2, 1981, pp. 263-293.
9. Benek, J.A., et al, "A 3-D Chimera Grid Embedding Technique," AIAA Paper No. 85-1523, July 1985.
10. Kayser, L.D. and Whiton, F., "Surface Pressure Measurements on a Boattailed Projectile Shape at Transonic Speeds," U.S. Army Ballistic Research Laboratory, ARBRL-MR-03161, March 1982. (AD A113520)
11. Kayser, L.D., "Base Pressure Measurements on a Projectile Shape at Mach Numbers from 0.91 to 1.20," U.S. Army Ballistic Research Laboratory, ARBRL-MR-03353, April 1984. (AD A141341)
12. Baldwin, B.S. and Lomax, H., "Thin Layer Approximation and Algebraic Model for Separated Turbulent Flows," AIAA Paper No. 78-257, 1978.

DISTRIBUTION LIST

<u>No. of Copies</u>	<u>Organization</u>	<u>No. of Copies</u>	<u>Organization</u>
12	Administrator Defense Technical Info Center ATTN: DTIC-FDAC Cameron Station, Bldg 5 Alexandria, VA 22304-6145	1	Director US Army Aviation Research and Technology Activity Ames Research Center Moffett Field, CA 94035-1099
1	HQDA DAMA-ART-M Washington, DC 20310	10	C.I.A OIR/DB/Standard GE47 HQ Washington, DC 20505
1	Commander US Army Materiel Command ATTN: AMCDRA-ST 5001 Eisenhower Avenue Alexandria, VA 22333-0001	1	Commander US Army Communications - Electronics Command ATTN: AMSEL-ED Fort Monmouth, NJ 07703-5301
3	Commander US Army Armament Research, Development and Engineering Center ATTN: SMCAR-MSI SMCAR-LCA-F/Klein Hudgins Dover, NJ 07801-5001	1	Commander CECOM R&D Technical Library ATTN: AMSEL-IM-L (Reports Section) B.2700 Fort Monmouth, NJ 07703-5000
1	Commander US Army Armament Research, Development and Engineering Center ATTN: SMCAR-TDC Dover, NJ 07801-5001	1	Commander US Army Missile Command Research, Development, and Engineering Center ATTN: AMSMI-RD Redstone Arsenal, AL 35898-5230
1	Commander US AMCCOM ARDEC CCAC Benet Weapons Laboratory ATTN: SMCAR-CCB-TL Watervliet, NY 12189-4050	1	Director US Army Missile and Space Intelligence Center ATTN: AIAMS-YDL Redstone Arsenal, AL 35898-5500
1	Commander US Army Armament, Munitions and Chemical Command ATTN: AMSMC-IMP-L Rock Island, IL 61299-7300	1	Commander US Army Tank Automotive Command ATTN: AMSTA-TSL Warren, MI 48397-5000
1	Commander US Army Aviation Systems Command ATTN: AMSAV-FS 4300 Goodfellow Blvd. St. Louis, MO 63120-1798	1	Director US Army TRADOC Analysis Center ATTN: ATOR-TSL White Sands Missile Range, NM 88002-5502

DISTRIBUTION LIST

<u>No. of Copies</u>	<u>Organization</u>	<u>No. of Copies</u>	<u>Organization</u>
2	Commander US Naval Surface Weapons Center ATTN: Dr. T. Clare, Code DK20 Dr. F. Moore Dahlgren, VA 22448-5000	1	Pennsylvania State University Department of Aerospace Engineering ATTN: Dr. G. S. Dulikravich University Park, PA 16802
1	Commandant US Army Infantry School ATTN: ATSH-CD-CS-OR Fort Benning, GA 31905-5400	1	University of Florida Dept. of Engineering Sciences College of Engineering ATTN: Prof. C. C. Hsu Gainesville, FL 32611
1	Commander US Army Development and Employment Agency ATTN: MODE-ORO Fort Lewis, WA 98433-5000	1	University of Maryland Department of Aerospace Engineering ATTN: Dr. J.D. Anderson, Jr. College Park, MD 20742
3	Director NASA Ames Research Center ATTN: MS-202-1/Pulliam MS-258-1/Steiger Schiff Moffett Field, CA 94035	1	University of Illinois at Urbana Champaign Department of Mechanical & Industrial Engineering ATTN: Prof. W. L. Chow Urbana, IL 61801
1	AFWL/SUL Kirtland AFB, NM 87117	1	University of Notre Dame Department of Aeronautical & Mechanical Engineering ATTN: Prof. T.J. Mueller Notre Dame, IN 46556
1	Air Force Armament Laboratory ATTN: AFATL/DLODL (Tech Info Center) Eglin AFB, FL 32542-5000	1	University of Texas Department of Aerospace Engineering & Engineering Mechanics ATTN: Dr. D.S. Dolling Austin, Texas 78712-1055
2	Sandia National Laboratories ATTN: Dr. W.L. Oberkampf Dr. F. Blottner Division 1636 Albuquerque, NM 87185		
1	AEDC Calspan Field Services ATTN: MS 600 (Dr. John Benek) AAFS, TN 37389		<u>Aberdeen Proving Ground</u>
1	University of California, Davis Department of Mechanical Engineering ATTN: Prof. H.A. Dwyer Davis, CA 95616		Dir, USAMSAA ATTN: AMXSY-D AMXSY-MP, H. Cohen
			Cdr, USATECOM ATTN: AMSTE-SI-F
			Cdr, CRDC, AMCCOM ATTN: SMCCR-RSP-A SMCCR-MU SMCCR-SPS-IL

### USER EVALUATION SHEET/CHANGE OF ADDRESS

This Laboratory undertakes a continuing effort to improve the quality of the reports it publishes. Your comments/answers to the items/questions below will aid us in our efforts.

1. BRL Report Number \_\_\_\_\_ Date of Report \_\_\_\_\_

2. Date Report Received \_\_\_\_\_

3. Does this report satisfy a need? (Comment on purpose, related project, or other area of interest for which the report will be used.)  
\_\_\_\_\_  
\_\_\_\_\_

4. How specifically, is the report being used? (Information source, design data, procedure, source of ideas, etc.)  
\_\_\_\_\_  
\_\_\_\_\_

5. Has the information in this report led to any quantitative savings as far as man-hours or dollars saved, operating costs avoided or efficiencies achieved, etc? If so, please elaborate.  
\_\_\_\_\_  
\_\_\_\_\_

6. General Comments. What do you think should be changed to improve future reports? (Indicate changes to organization, technical content, format, etc.)  
\_\_\_\_\_  
\_\_\_\_\_

Name \_\_\_\_\_

CURRENT Organization \_\_\_\_\_  
ADDRESS \_\_\_\_\_

Address \_\_\_\_\_

City, State, Zip \_\_\_\_\_

7. If indicating a Change of Address or Address Correction, please provide the New or Correct Address in Block 6 above and the Old or Incorrect address below.

Name \_\_\_\_\_

OLD Organization \_\_\_\_\_  
ADDRESS \_\_\_\_\_

Address \_\_\_\_\_

City, State, Zip \_\_\_\_\_

(Remove this sheet, fold as indicated, staple or tape closed, and mail.)

— — — — — FOLD HERE — — — — —

Director  
US Army Ballistic Research Laboratory  
ATTN: DRXBR-OD-ST  
Aberdeen Proving Ground, MD 21005-5066

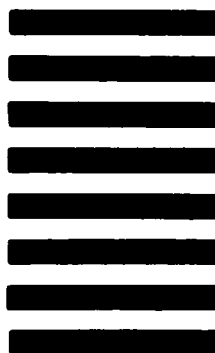


NO POSTAGE  
NECESSARY  
IF MAILED  
IN THE  
UNITED STATES

OFFICIAL BUSINESS  
PENALTY FOR PRIVATE USE. \$300

**BUSINESS REPLY MAIL**  
FIRST CLASS PERMIT NO 12062 WASHINGTON, DC  
POSTAGE WILL BE PAID BY DEPARTMENT OF THE ARMY

Director  
US Army Ballistic Research Laboratory  
ATTN: DRXBR-OD-ST  
Aberdeen Proving Ground, MD 21005-9989



— — — — — FOLD HERE — — — — —

END

DATE

FILED

8-88

DTIC